Experimental and numerical investigations of aerodynamic loads and 3D flow over non-rotating MEXICO blades

Zhang, Ye; Gillebaart, Thijs; van Zuijlen, Alexander; van Bussel, Gerard; Bijl, Hester

DOI
10.1002/we.2025

Publication date
2017

Document Version
Final published version

Published in
Wind Energy

Wind Energy

WIND ENERGY
Wind Energ. (2016)
Published online in Wiley Online Library (wileyonlinelibrary.com). DOI: 10.1002/we.2025

RESEARCH ARTICLE

Experimental and numerical investigations of aerodynamic loads and 3D flow over non-rotating MEXICO blades

Ye Zhang, Thijs Gillebaart, Alexander van Zuijlen, Gerard van Bussel and Hester Bijl

DUWIND, Faculty of Aerospace Engineering, Delft University of Technology, Kluyverweg 1, 2629HS, Delft, The Netherlands

ABSTRACT

This paper presents the experimental and numerical study on MEXICO wind turbine blades. Previous work by other researchers shows that large deviations exist in the loads comparison between numerical predictions and experimental data for the rotating MEXICO wind turbine. To reduce complexities and uncertainties, a non-rotating experimental campaign has been carried out on MEXICO blades Delft University of Technology. In this new measurement, quasi-2D aerodynamic characteristics of MEXICO blades on three spanwise sections are measured at different inflow velocities and angles of attack. Additionally, RANS simulations are performed with OpenFOAM-2.1.1 to compare numerical results against measured data. The comparison and analysis of aerodynamic loads on the blade, where three different airfoil families and geometrical transition regions are used, show that for attached flow condition, RANS computation predicts excellent pressure distribution on the NACA airfoil section ($r/R = 0.92$) and good agreement is observed on the DU ($r/R = 0.35$) and RISØ ($r/R = 0.60$) airfoil sections. Unexpected aerodynamic characteristics are observed at the intermediate transition regions connecting the RISØ and DU airfoils, where sudden lift force drop is found at the radial position $r/R = 0.55$. Through numerical flow visualization, large-scale vortical structures are observed on the suction side of the blade near the mid-span. Moreover, counter-rotating vortices are generated behind the blade at locations where unexpected loads occurs. Consequently, the RISØ airfoil could not give expected 2D aerodynamic characteristics because of upwash/downwash effects induced by these counter-rotating vortices, which make 3D effects play an important role in numerical modeling when calculating the aerodynamic loads for MEXICO rotor. ©2016 The Authors Wind Energy Published by John Wiley & Sons Ltd

KEYWORDS

3D effects; aerodynamic loads; non-rotating blades; MEXICO wind turbine; OpenFOAM

Correspondence

Y. Zhang, DUWIND, Faculty of Aerospace Engineering, Delft University of Technology, Kluyverweg 1, 2629HS, Delft, The Netherlands.
E-mail: ye.zhang@tudelft.nl

Received 25 July 2015; Revised 11 May 2016; Accepted 4 August 2016

1. INTRODUCTION

In recent years, with increased use of wind energy, the size and complexity of modern commercial horizontal axis wind turbines are increasing rapidly. In order to avoid turbine failure and decrease the manufacturing cost for large wind turbines, reliable and accurate aerodynamic models are crucial and required at the design process. To validate and improve these aerodynamic models, several high-quality experiments have been conducted over the past decade to provide a reliable experimental database. A classical experiment is full-scale test of the National Renewable Energy Laboratory (NREL) unsteady aerodynamics experiment phase VI, which measured a 10 m diameter, stall-regulated horizontal axis wind turbines in the NASA Ames wind tunnel (24.4 m × 36.6 m) in 2000. A two-bladed turbine with twisted and tapered blades was tested in both upwind and downwind rotor configurations. The rotating blade pressure distribution at five blade spanwise sections, angle of attack and inflow dynamic pressure were measured during the experiment.[1] Another experiment is Model EXperiment In Controlled cOndition (MEXICO), conducted in 2006 in the large-scale low-speed facility of the

German Dutch Wind tunnel Organization.[2] In this experiment, a 4.5 m diameter, three-bladed, pitch controlled wind turbine rotor model was used, and loads on the rotating blades were measured by Kulite pressure transducers. Additionally, in the MEXICO experiment, the wind turbine wake was measured in detail using particle image velocimetry technology. The combination of measured blade loads and wake flow field resulted in a comprehensive database for validation of aerodynamic models. Because of the complex physics of wind turbine aerodynamics, in some cases, the aerodynamic models have difficulty in calculating the turbine performance and loads accurately. The blind comparisons between experiment and aerodynamic models show large discrepancy when these models are not tuned to the experiment. In the NREL experiment, the comparison indicates that even at easy-to-predict wind turbine operation conditions, which are no-yaw, steady-state flow, the derivation ranges from 25% to 175% for turbine power prediction. Blade bending force prediction ranges from 85% to 150% compared with the measurement.[3] The comparison becomes even worse at higher wind speed. In the MEXICO experiment, the final conclusion states that all loads along the blade are consistently over predicted by most of aerodynamic models with the same level of magnitude as in the NREL experiment. At the stall condition, although the computational fluid dynamic (CFD) models give better prediction compared with other engineering models (BEM, lifting line), still considerable deviations can be found in the comparison. These differences still cannot be fully explained.[4–6]

Therefore, in order to better understand the reason of this discrepancy in the comparison between measurements and numerical results for the MEXICO experiment, this study makes an in-depth experimental and numerical comparison of the MEXICO blades. To reduce the complexity of the flow and uncertainties in the experiment, every MEXICO blade is measured separately under parked (non-rotating) conditions.

Many CFD studies have focused on simulating the flow over standstill wind turbine. Sørensen *et al.*[7] compared measured and computed pressure distribution and integrated forces for two rotors' blades. The comparisons showed a better loads prediction capability of Menter's $k-\omega$ SST turbulence model compared with the original Wilcox's $k-\omega$ turbulence model. Furthermore, it was concluded that the tangential forces in the attached flow conditions are difficult to predict correctly when fully turbulent flow is assumed. In a numerical study of the MEXICO rotor by CENER*, it was concluded that parked cases are harder to predict than expected: both because of the large twist of the blades and because of the uncertainties in standstill measurement data, such as erroneous pressure transducer measurements on the inboard part (25%R and 35%R) of the blades.[4] The author recommended more CFD simulations to be performed and other turbulence models to be considered for better predicting the aerodynamic loads at standstill conditions. However, in our non-rotating experiment, each blade of the MEXICO rotor can be measured on three radial sections in the well-controlled flow condition. CFD simulations are expected to cope with the quasi-2D aerodynamics without too much effort in comparisons with the experimental measurements. Indeed, previous simulations[8] on the non-rotating MEXICO blade, at fully attached, massively separated and stall conditions, demonstrate that Reynolds-averaged Navier–Stokes simulations with Menter's $k-\omega$ SST turbulence model shows good agreement with the experiment for fully attached flow at low angles of attack.

Different from previous work,[8] the current paper focuses on detailed investigation of the MEXICO blade sectional loading and 3D effects. This paper is organized as follows: first, the setup of non-rotating MEXICO blades experiment, performed in the low-speed low-turbulence (LTT) wind tunnel at Delft University of Technology, is briefly described. Second, CFD simulations are carried out to understand further about aerodynamic loads and flow behavior on the non-rotating MEXICO blades. The numerical results concentrate on the comparisons of the pressure distribution at three radial sections with the experimental measurements. In addition, the flow topology predicted by CFD simulation is also compared with oil flow visualization in the experiment. Afterwards, the numerical investigations of the aerodynamic loads and 3D flow around the non-rotating blades give more insight into the MEXICO blades.

2. METHODS

2.1. Experimental approach

2.1.1. Wind tunnel, the model and the apparatus.

The wind tunnel measurements on the non-rotating MEXICO blades are performed in the LTT wind tunnel at Delft University of Technology. The LTT is a closed return wind tunnel with an exchangeable, octagonal test section 2.60 m long, 1.80 m wide and 1.25 m high. The free-stream turbulence intensity in the test section varies from 0.015% at 20 m s^{-1} to 0.10% at 120 m s^{-1}. The inflow velocity is kept at 35 and 60 m s^{-1} in this experiment.

The models measured in the experiment are the blades of a three-bladed, horizontal axis MEXICO wind turbine rotor. The blade is tapered with a length of 2.04 m. Three different airfoil profiles exist along the span of the blade. From the root to the tip, they are the DU91-W2-250 airfoil from 20% to 45.6% span, the RISØ-A1-21 airfoil from 54.4% to 65.6% span and the NACA 64-418 airfoil from 74.4% span to the tip. The remaining parts are the intermediate regions connecting two

*National Renewable Energy Center of Spain, one collaboration partner in the MEXICO project.

DOI: 10.1002/we

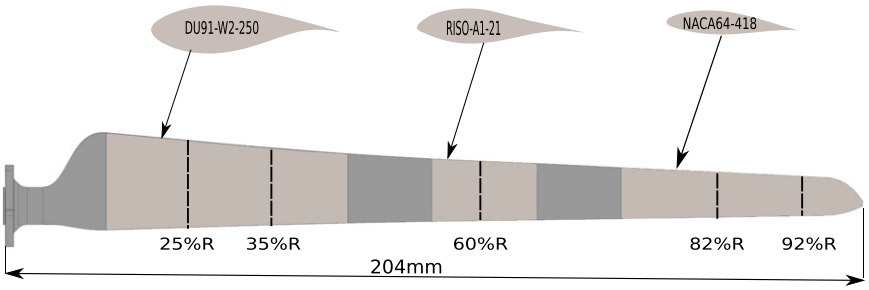

Figure 1. Airfoil distributions over the span of the MEXICO blade.

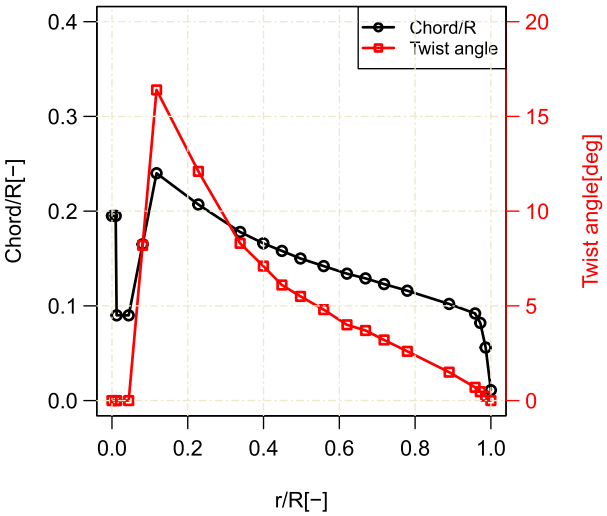

Figure 2. Chord and twist distribution of the MEXICO blade.

adjacent airfoil profiles and lofted with tengency. Figure 1 shows the airfoil distributions over the blade span. The chord and twist distribution of the MEXICO blade is also illustrated in Figure 2.

The apparatus used in the experiment are Kulite pressure transducers, wake rake and oil. The usage of the technical equipments are itemized as follows:

- There are 148 Kulite pressure transducers in total on the three blades, distributed over five different instrumented sections. These transducers measure the pressure distribution over all tested airfoil sections, which are 25%R and 35%R spanwise locations of blade 1, 60%R spanwise location of blade 2, and 82%R and 92%R spanwise locations of blade 3. Before the measurement, a static calibration of Kulite pressure transducers is performed, covering the pressure range observed throughout the measurement campaign.
- The wake rake is used to measure the velocity deficit behind the blades with 16 static and 67 total pressure tubes mounted on a spar. After that, the sectional total drag can be determined.
- The flow topology over the blade surface such as laminar/turbulence transition, flow separation, and 3D effects can be clearly seen with oil flow techniques.

2.1.2. Experimental setup and procedure.

Each blade is mounted vertically in the test section and because the blades' span is longer than the test section height, two experimental setups are used. As shown in Figure 3, the pressure at 35% span location is measured on blade 1 with the outboard part of the blade outside of the test section. The pressure at 60% and 92% span is measured on blade 2 and blade 3, respectively, which are mounted with a free blade tip, see Figure 4. Zigzag tape is applied on both pressure and suction sides at 10% chord to promote transition and avoid free laminar to turbulent transition.

In order to keep the chord-based Reynolds number Re_c identical as the previous rotating experiment, the inflow velocities are chosen as 35 and 60 m s^{-1} to match Re_c. The quasi-2D aerodynamic characteristics on these three test sections are obtained at a range of angles of attack, from $-20°$ to $20°$. The rotating table at the top of the test section can adjust the tip

Figure 3. Experimental setup of the model: the MEXICO blade 1.

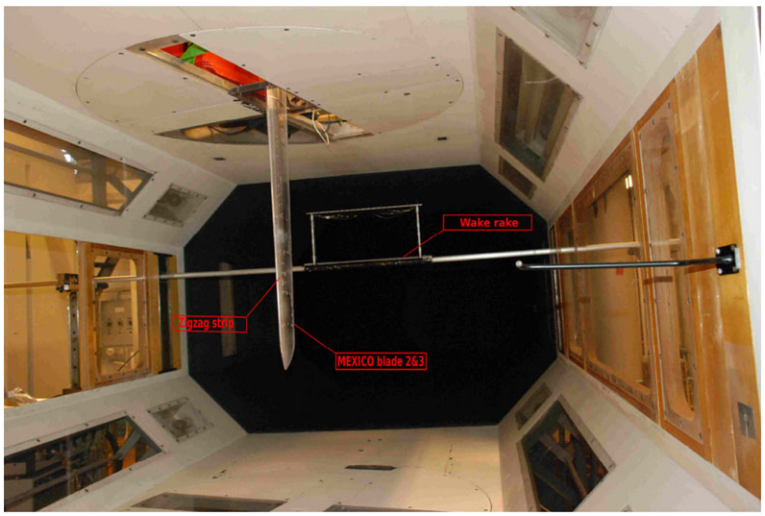

Figure 4. Experimental setup of the models: the MEXICO blades 2 and 3.

Table I. Parameters of some cases to be compared.

Blade number	No.1	No.2	No.3
Measured section[-]	35%R	60%R	92%R
Geometric angle of attack α[°]	1, 5, 8	0, 5, 8	2, 5, 8
Inflow velocity[m s^{-1}]	35	35	60
Reynolds number Re_C[-]	4.6×10^5	3.4×10^5	4.0×10^5

pitch angle of the blades, in such a way that the desired geometric angle of attack α (defined as the angle between inflow direction and chord line) is obtained. Calibrated Kulite pressure transducers are used to measure the sectional pressure distribution. By integrating the pressure, the lift force and the pressure drag can be calculated afterwards. Wake rake measurements are used to determine the sectional total drag to estimate viscous drag. After the pressure measurements, an oil flow measurement is carried out to visualize the flow phenomena over blade 3 surface. Table I summaries the experimental configurations that will be used for validation of the CFD simulations.

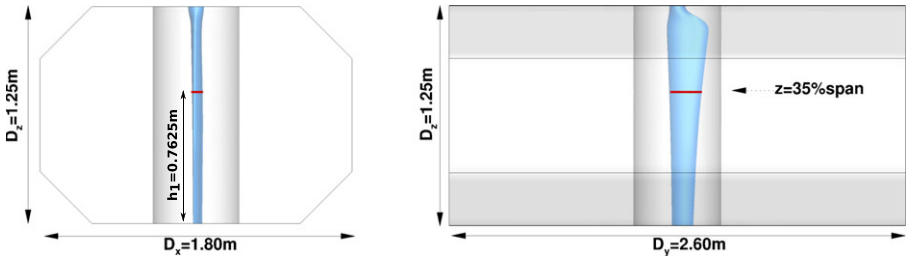

Figure 5. Numerical setup of the model: the MEXICO blade 1.[8]

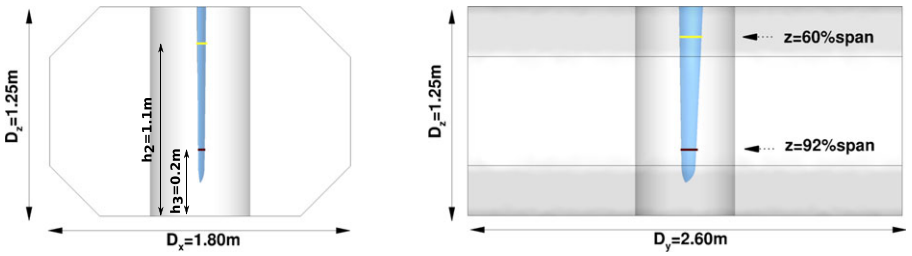

Figure 6. Numerical setup of the models: the MEXICO blades 2 and 3.[8]

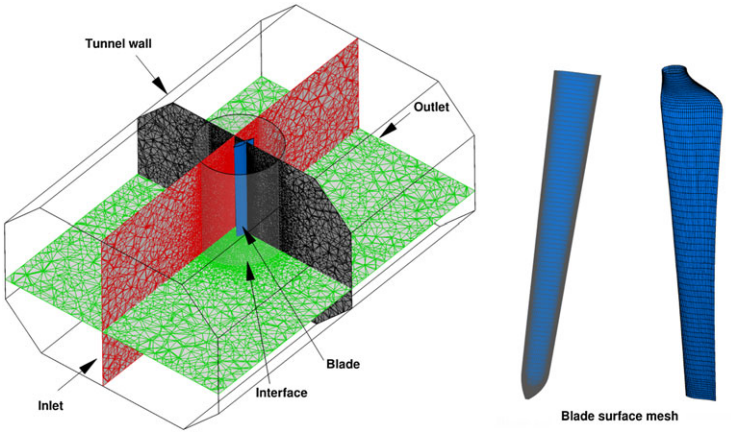

Figure 7. Schematic of the computational domain and blade surface mesh.

2.2. Numerical approach

2.2.1. Geometry modeling and grid generation.

The CFD simulations are performed on a computational domain that is identical to the experimental setup. The whole wind tunnel test section including wind tunnel walls are modeled, not only the blades. Therefore, the blockage effects present are also considered by CFD. Similar to the experimental setups, there are two different computational domains, one with the blade extending from top to bottom of the test section (Figure 5) and one with a free blade tip (Figure 6). A cylindrical domain which includes the blade is created, and it can be rotated to the desired pitch angle to match the geometric angle of attack α corresponding to the measurement. The measured sections are located at a distance from the bottom of the test section wall: 0.7625, 1.1 and 0.2 m, respectively.

A hybrid mesh strategy is used for generating the CFD mesh. Structured hexahedral grid is applied near the blade where the viscous flow in the boundary layer is solved with high-grid resolution. The outer region is filled with a coarse, unstructured mesh. The non-dimensional value y^+ is below 2, and approximately, 20 cell layers are used in the viscous region. An illustration of the mesh and blade surface mesh is given in Figure 7. Three different grid levels are generated for examining the spatial convergence in total (see Table II for details).

Table II. The characteristics of three different grids.

Grid Characteristic	Coarse	Medium	Fine
Chordwise nodes	90	120	150
Spanwise nodes	80	100	125
First grid spacing (mm)	0.015	0.009	0.005
y^+	1.5	1.0	0.5
Maximum skewness	1.1	0.97	1.05
Maximum orthogonality	65.8	65.6	66.1
Maximum aspect ratio	1675	3543	4191
Total cells	5.26×10^5	8.74×10^5	1.45×10^6

2.2.2. Assumptions, boundary conditions and numerical schemes.

To model and investigate the flow physics over the blades, we propose some assumptions to simplify the numerical modeling.

- To save the computational time, steady-state Navier–Stokes solver with Reynolds-averaged Navier–Stokes turbulence modeling approach is chosen for predicting the cases where the flow is attached in the experiment.
- Considering simplification of flow physics, fully turbulent flow over the blades is assumed. Hence, laminar-to-turbulent transition is not considered in the simulation.
- Zigzag stripe has little influence on the integrated pressure when the flow is still attached. Therefore, the geometry of zigzag is not modeled for the CFD model.
- A rectangular wind tunnel wall is employed in the CFD geometry, since the side walls of the tunnel in the experiment are designed with slightly diverging shape to compensate for the displacement effect of the tunnel wall boundary layers. In addition, with the assumption that viscous effects on the wall are not expected to have a major influence on the pressure distribution, especially for the sections (35%R and 92%R) far from the wall, the boundary layer developed at the wind tunnel wall is not resolved in CFD in order to decrease the grid size.

Assuming viscous effect from the wind tunnel wall is neglected, the slip boundary condition is chosen at the wind tunnel wall. The boundary condition for the velocity field is applied as Dirichlet boundary condition with a constant inflow velocity at the inlet boundary and Neumann boundary condition at the outlet. The pressure is set as a Neumann boundary condition at all boundaries. The solid blade surface is enforced as no-slip boundary condition. An arbitrary mesh interface[9] boundary condition is used between the two adjacent mesh domains. The free-stream turbulence intensity I is estimated as 0.06% inflow velocity V_∞:

$$I = \frac{u'}{V_\infty} = 0.06\% \tag{1}$$

where $u' = \sqrt{\frac{2}{3}k}$ is the root-mean-square of the turbulent velocity fluctuations. Based on the turbulence intensity, the turbulent variables k and ω can be calculated as the reference,[10] and the boundary conditions are specified in the simulation. The order of accuracy of selected numerical schemes for N-S equations discretization is second-order upwind. SIMPLE algorithm[11] is used to correct the pressure in the iterations.

3. RESULTS AND DISCUSSION

3.1. Grid refinement study

Figures 8 and 9 show the results of grid refinement study based on three different grid levels. In the figures, the pressure and skin friction coefficient distribution on the DU airfoil section at 35% span are plotted with a geometric angle of attack $\alpha = 8°$, which is symbolized by $\alpha_{0.35} = 8°$. These two variables are defined as

$$C_p = \frac{p - p_0}{\frac{1}{2}\rho V_\infty^2} \tag{2}$$

and

$$C_f = \frac{\tau}{\frac{1}{2}\rho V_\infty^2} \tag{3}$$

where p is the static pressure, p_0 is the reference pressure, V_∞ is the inflow velocity, ρ is the fluid density, and τ is the wall shear stress.

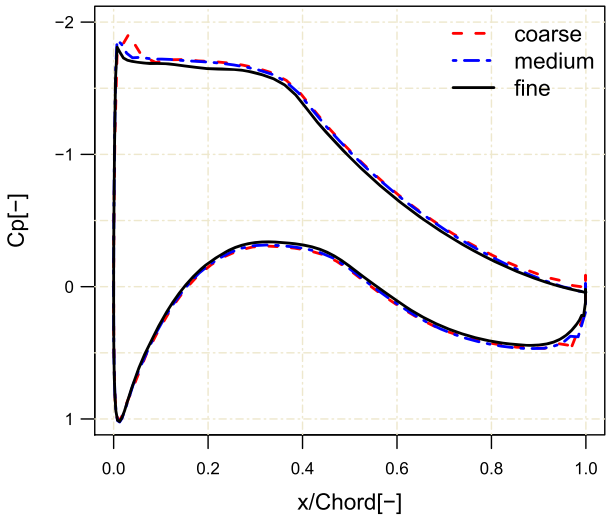

Figure 8. Grid convergence study, Cp comparison between coarse, medium and fine grids.

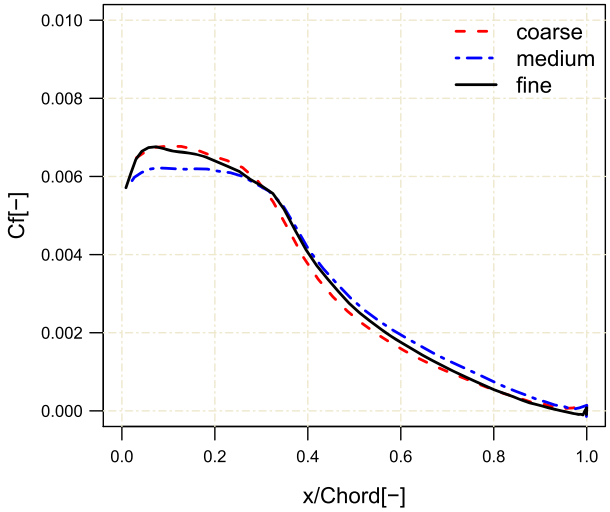

Figure 9. Grid convergence study, Cf comparison between coarse, medium and fine grids on the suction side.

As the grid density increases, the pressure tends to a converged solution, and only small differences can be seen close to the suction peak and trailing edge between the coarse and fine mesh solution, with a difference 6.7% integral lift force. The skin friction coefficient is, however, more sensitive to the mesh resolution and does not seem to present a monotonic behavior. C_f on the medium mesh is underestimated between $x/c = 0.0$ and $x/c = 0.30$ compared with C_f on the coarse and fine mesh, but the difference between the medium mesh and fine mesh is about 6% integral drag force, which is acceptable in our simulation. Therefore, the solutions on the fine mesh are considered to achieve spatial convergence, and the numerical results presented subsequently are based on the fine mesh.

3.2. Pressure comparison

DU section at 35 m s^{-1}, 35% span

Figure 10 presents the comparison of the calculated and measured pressure distribution at 35% spanwise section of blade 1. At this section, the airfoil profile is the DU airfoil with 25% thickness. The geometric angles of attack are $\alpha_{0.35} = 1°, 5°$, and 8°. Overall speaking, good agreement within less than 10% $\triangle C_p$ ($\triangle C_p$ is defined as C_{Pmax} - C_{Pmin} with pressure sensor value) difference can be obtained between CFD results and experiment except for several locations, where the pressure sensor values are indicated by red square. The pressure transducers on the suction side which are located at $x/c = 0.053$

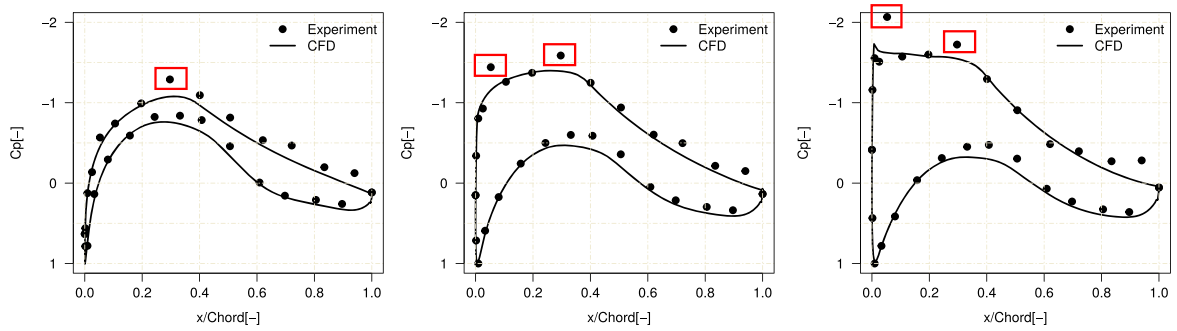

Figure 10. Pressure coefficient comparison of the DU airfoil at 35% spanwise section of blade 1: $\alpha_{0.35}$ = 1°, 5° and 8° with inflow velocity V_∞ =35 m s^{-1}, $Re_c = 4.6 \times 10^5$.

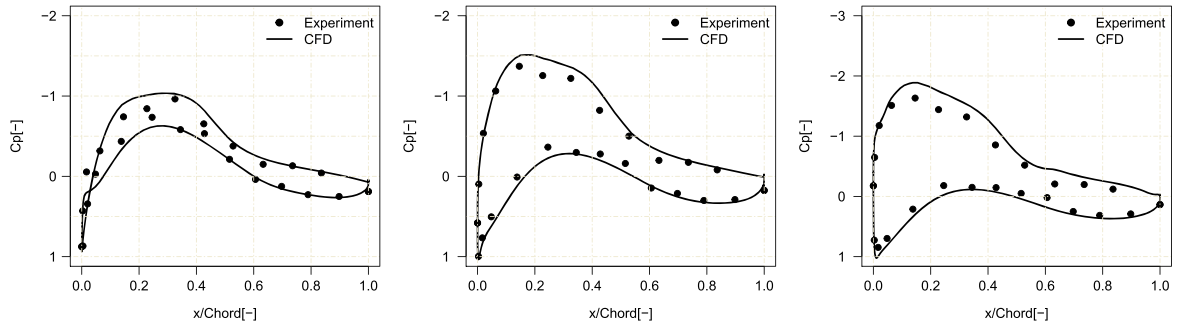

Figure 11. Pressure coefficient comparison of the RISØ airfoil at 60% spanwise section of blade 2: $\alpha_{0.60}$ = 0°, 5° and 8° with inflow velocity V_∞ = 35 m s^{-1}, $Re_c = 3.4 \times 10^5$.

and $x/c = 0.3$ show unexpected pressures for the $\alpha_{0.35} = 5°$ and $\alpha_{0.35} = 8°$ cases, while at $\alpha_{0.35} = 1°$, the pressure sensor at $x/c = 0.053$ shows expected value. This phenomenon has been pointed out both in the rotating MEXICO wind turbine experiment and CFD simulations by other researchers, see Schepers and Snel[2] and Bechmann *et al.*[6] A possible explanation has been attributed to some malfunctioning sensors at that position. Although the pressure sensors were calibrated before the non-rotating experiment, it still shows obviously unexpected pressure during the measurement. Another difference can been seen near the trailing edge on the suction side, when the geometric angle of attack increases from $\alpha_{0.35} = 5°$ to $\alpha_{0.35} = 8°$. The measured pressure indicates that the flow separates at the trailing edge in the experiment, which is not captured by the current simulation.

Regarding the pressure comparison on the pressure side, CFD results show correct pressure distribution trend as the experimental measurement. However, consistent pressure overprediction is found over the pressure side between $x/c = 0.3$ and $x/c = 0.5$ for all cases. Considering the pressure in the region before $x/c = 0.3$ and after $x/c = 0.5$ is predicted correctly, and the possible reason for the overprediction would be slight geometry deviation between the experimental model and modeled CFD geometry.

RISØ section at 35 m s^{-1}, 60% span

At 60% spanwise section of blade 2 with RISØ airfoil, the CFD results and experimental measurements of pressure distribution are compared in Figure 11. The maximum difference between CFD and experiment is less than 10%$\triangle C_p$ for all the measured points. On the pressure side, good agreement is obtained for all pressure sensors except for the ones between $x/c = 0.146$ and $x/c = 0.344$. Similar behavior that over predicts the pressure is observed as the case for the DU airfoil section. For all the cases $\alpha_{0.60} = 0°$, 5°, and 8°, on the suction side, the numerical results always underpredict the pressure compared with the measurement. Therefore, the integrated sectional lift force is expected to be over predicted for the RISØ airfoil section. Because the section considered here is relative close to the tunnel wall, there will be secondary vorticity shedding at the wall corner, which could explain the measured lift that is smaller than the CFD results.

NACA section at 60 m s^{-1}, 92% span

Figure 12 shows the pressure comparison at 92% spanwise section of blade 3. The NACA 64-418 airfoil profile is applied at this location, which is close to the tip of the blade. Even though the flow is complex and challenges CFD simulations due to the existence of the tip vortex effects, but as seen in the figure, at the three angles of attack $\alpha_{0.92} = 2°$, 5° and 8°, all

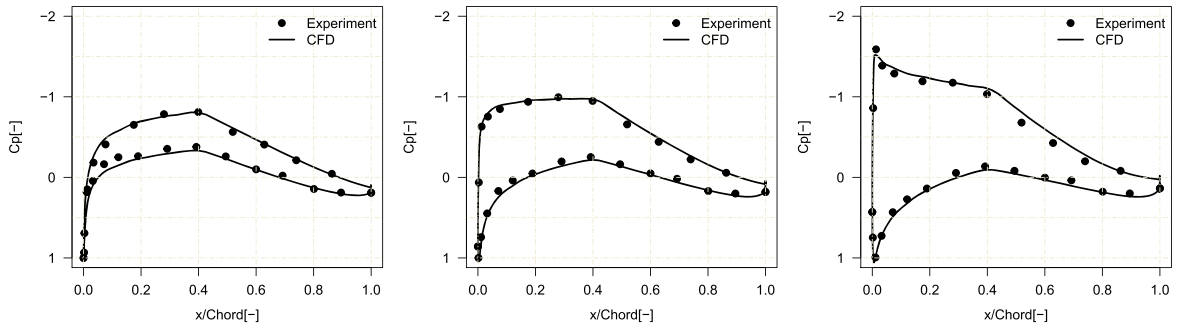

Figure 12. Pressure coefficient comparison of the NACA airfoil at 92% spanwise section of blade 3: $\alpha_{0.92}$ = 2°, 5° and 8° with inflow velocity $V_\infty = 60$ m s^{-1}, $Re_c = 4.0 \times 10^5$.

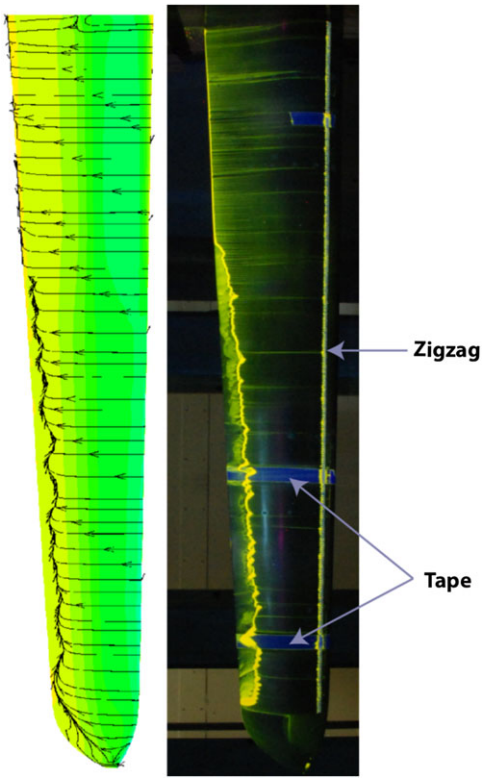

Figure 13. Flow topology comparison between CFD limiting streamline and experimental oil flow visualization, flow is from right to left, angle of attack $\alpha_{0.82} = 8°$, CFD result is colored by the pressure.

the computations give excellent agreement with experimental data. For each case, the pressure distribution over the NACA airfoil is well captured by the simulation.

3.3. Oil flow comparison

In the experiment, the flow over the blade was visualized by the oil flow technique for blade 3 at the inflow velocity V_∞ =60 m s^{-1}. In Figure 13, the right image shows the oil flow visualization over the blade surface for the geometric angle of attack $\alpha_{0.82} = 8°$ at 82% spanwise section. The flow comes from right to left. The zigzag stripe is used to trigger the flow turbulent at 10% chord and can be clearly seen in the oil flow image, except for the blade tip, where no stripe was applied. The horizontally pasted tape was placed on the pressure sensors at the sections 60%, 82%, and 92% of the blade to prevent the pressure sensors from being damaged by the oil. The bright line indicates the location where the flow starts to separate. It can be seen that the flow remains fully attached at the root of the measured model. With the increased angle

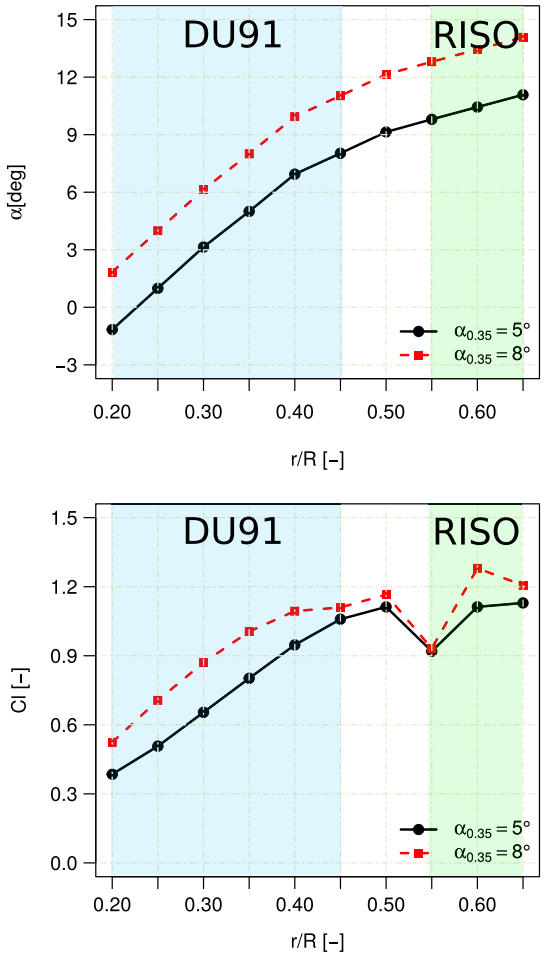

Figure 14. Distribution of geometric angle of attack and lift coefficient from CFD results along blade 1.

of attack towards to the tip, the flow starts to separate near the trailing edge from $r/R \approx 0.70$ to the tip. Compared with the simulated limiting streamline visualization in the left image, good flow topology agreement with respect to flow separation can be obtained between CFD and experimental oil flow measurement.

3.4. Aerodynamic loads calculation

Figure 14 shows the geometric angle of attack and corresponding numerical lift force coefficient distribution from the sections $r/R = 0.20$ to $r/R = 0.65$ of blade 1, where the geometric angle of attack at 35% spanwise section is $\alpha_{0.35} = 5°$ and 8°. At $\alpha_{0.35} = 5°$, with the increase of the radial position, higher lift force is obtained as a result of the increased geometric angle of attack, but a sudden lift drop at $r/R = 0.55$ is observed. When $\alpha_{0.35}$ is increased to 8°, the lift force increases on all different sections as expected, except for $r/R = 0.55$, which gives the same C_L value as the case $\alpha_{0.35} = 5°$. Moreover, the amount of the increased lift gradually decreases as the radial position transits from the DU airfoil to the intermediate region, which is from $r/R = 0.45$ to $r/R = 0.55$. The analysis reveals that the transition from the RiSØ arifoil family to the DU airfoil family does not transit smoothly enough which results in the unexpected lift distribution.

Similarly, Figure 15 presents the geometric angle of attack and the results of lift coefficient distribution of blade 2 from $r/R = 0.60$ to $r/R = 0.95$. From the lift distribution curve, it can be observed that the lift distribution is much smoother compared with blade 1 without sudden kink. Almost uniform lift increase over all the sections is obtained when the geometric angle of attack at 60% span increases from 5° to 8°. Near the tip region $r/R = 0.90 \sim 0.95$, due to the tip vortex effect, the significant lift reduction can be clearly seen for both $\alpha_{0.60} = 5°$ and $\alpha_{0.60} = 8°$ cases.

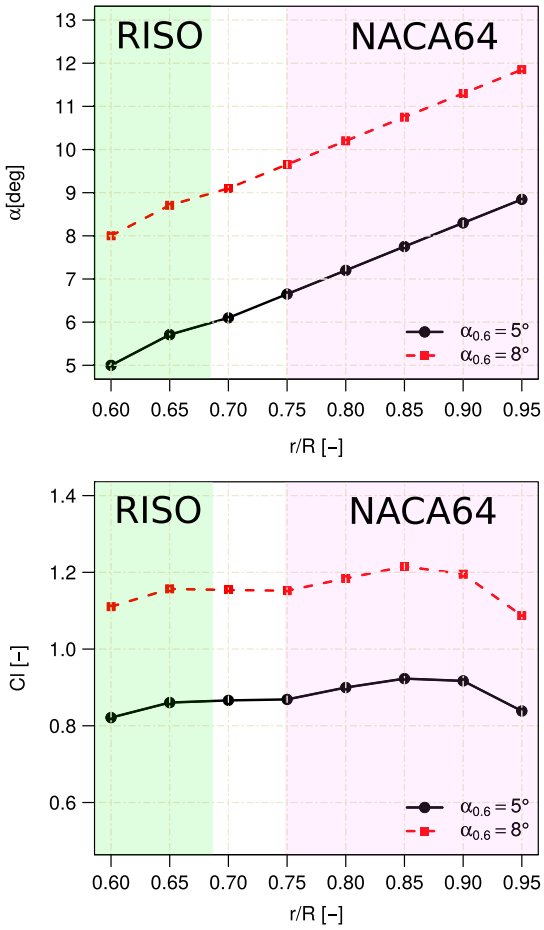

Figure 15. Distribution of geometric angle of attack and lift coefficient from CFD results along blade 2.

3.5. Flow field analysis

To better understand how this non-smooth transition mentioned in the previous section influences the flow in the particular region near $r/R = 0.55$, the Q criterion[12] is chosen to identify the vortical structures in the flow field. Q is the second invariant of the velocity gradient tensor ∇u, which can be written as follows:

$$Q = \frac{1}{2}\left(||\Omega||^2 - ||S||^2\right) \tag{4}$$

where S and Ω are the symmetric and antisymmetric parts of the tensor ∇u, and $||S|| = tr(SS^T)^{\frac{1}{2}}$, $||\Omega|| = tr(\Omega\Omega^T)^{\frac{1}{2}}$.

Three-dimensional large-scale vortical structures over blade 1 can be seen in Figures 16 and 17, colored by the vorticity magnitude. In Figure 16, large-scale vortical structures mainly appear at three locations, which are the two extremities close to the tunnel wall and the location $r/R = 0.55$. Clear large-scale vortex is seen at the root region of the blade, which can be attributed to the transition from the DU airfoil family to the cylinder. The other extremity with large-scale vortical structure caused by separated flow can be clearly seen at RISØ section. This section encounters high angle of attack because of blade twist. Apart from that, the influence of tunnel wall on the two regions could be considered as one additional reason for these large-scale vortical structures. The last position $r/R = 0.55$, as a consequence of non-smooth transition region where large-scale vortex emerges, is the transition region starting from the RISØ airfoil family to the DU airfoil family. When the angle of attack increases to $\alpha_{0.35} = 8°$, more vortical structures can be found towards to the root direction, which is close to the transition part as well. This region can be estimated from the loads calculation in Figure 14 from $r/R = 0.40$ to $r/R = 0.60$.

Based on the Prandtl lifting line theory,[13] the lift force over an airfoil can be calculated from

$$L = \rho V_\infty \Gamma \tag{5}$$

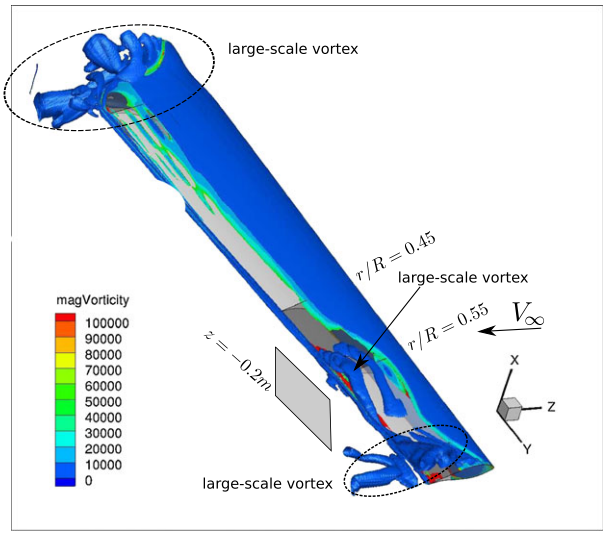

Figure 16. Three-dimensional visualization of vortical structure, isosurface $Q = 2 \times 10^5$ colored by vorticity magnitude, $\alpha_{0.35} = 5°$.

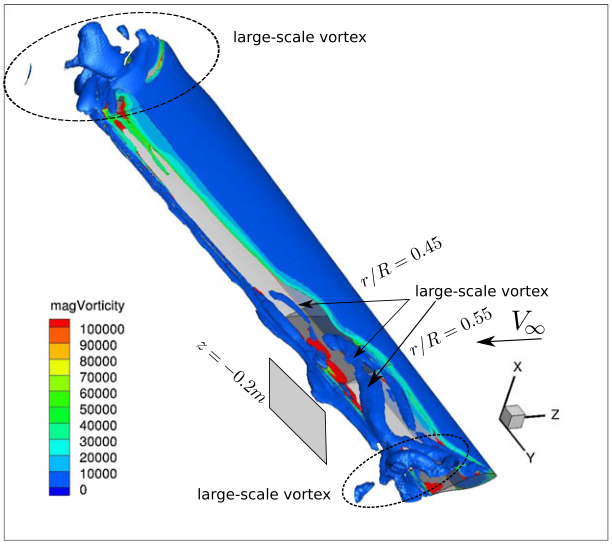

Figure 17. Three-dimensional visualization of vortical structure, isosurface $Q = 2 \times 10^5$ colored by vorticity magnitude, $\alpha_{0.35} = 8°$.

where Γ is the circulation over the airfoil section, representing the bound vortex strength. As a result of the sudden lift drop at $r/R = 0.55$, (see Figure 14), the rapid change in the circulation leads to the strength of the vortex at $r/R = 0.55$ to be smaller than other adjacent sections. Consequently, a pair of counter-rotating vortices are expected to be generated behind this position, which be discussed in detail in the following Section 3.6.

3.6. 3D effects

In order to quantify the influence of 3D flow on the airfoil aerodynamic characteristics, the lift curve derived from 3D CFD calculations and 2D experimental measurements are plotted together versus the geometric angles of attack in Figure 18. The geometric angle of attack corresponds to the angle between inflow direction and chord line of airfoil section both for the 2D and 3D cases. The chord based Re_c distribution along the blade span from 3D CFD calculations is also added on these graphs for better comparison. The available experimental 2D airfoil characteristics database in the MEXICO project is measured at $Re = 5 \times 10^5$ for the DU91 airfoil, and $Re = 1.6 \times 10^6$ for the RISØ airfoil, as shown in Figure 19.

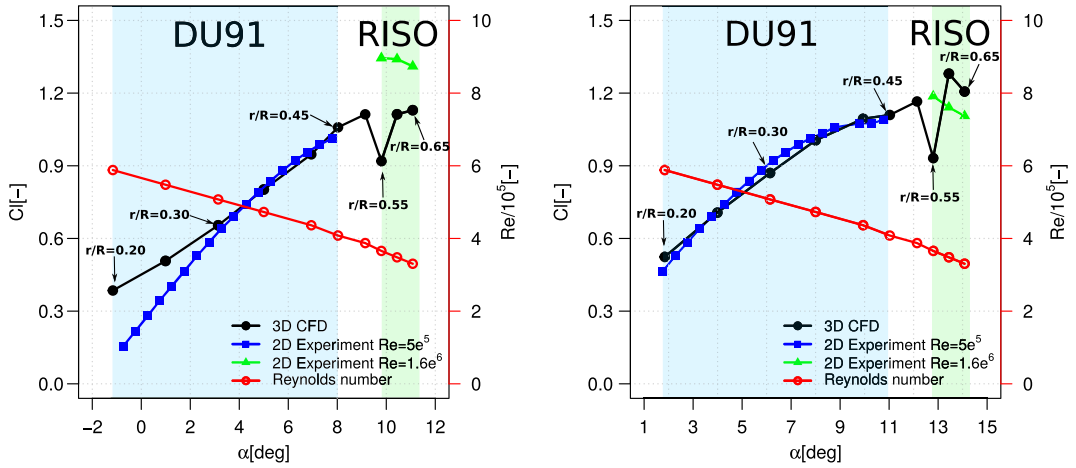

Figure 18. $C_L - \alpha$ comparison between 3D CFD calculation and 2D experimental data. $\alpha_{0.35} = 5^\circ$ (left) $\alpha_{0.35} = 8^\circ$ (right).

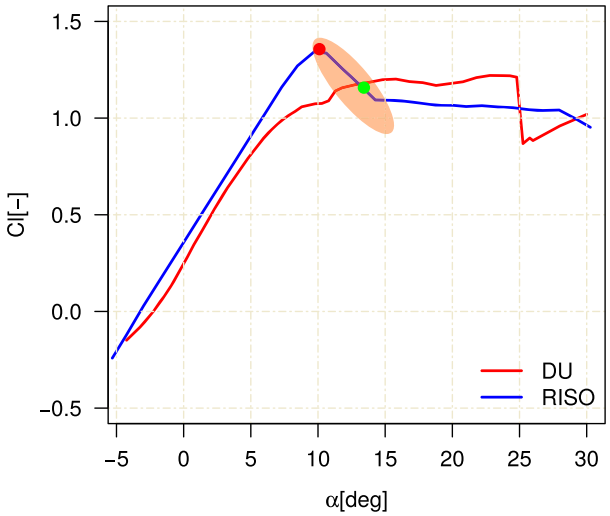

Figure 19. Measured $C_L - \alpha$ polar data for the DU ($Re = 5 \times 10^5$) and the RISØ ($Re = 1.6 \times 10^6$) airfoils.

When the geometric angle of attack $\alpha_{0.35} = 5^\circ$, the comparison shows that C_L values in the region $r/R = 0.30 \sim 0.45$ between 3D CFD results and 2D experimental measurements match very well. However, there are large differences at the root $r/R = 0.20 \sim 0.30$ and the mid-span $r/R = 0.55 \sim 0.65$. The 3D results give much higher C_L at the root but lower C_L at the mid-span, with maximum difference 69.8% and 46.2%. The differences can be explained by the influence of induced velocity that alters the local angle of attack. Figure 20 presents the contour of vertical and spanwise velocity distribution at the plane $z = -0.20$ m behind blade 1 to illustrate the induced effects. The velocity components correspond to X and Y directions, respectively, in Figures 16 and 20. At the root region $r/R = 0.20$, there are upwash effects induced by the velocity. These effects increase the local angle of attack and therefore results in higher C_L at this section in 3D calculations compared with 2D experimental data. At $r/R = 0.55$, because of the circulation difference as discussed earlier, a pair of counter-rotating vortices are observed near the same radial position in the plane $z = -0.2$ m (see Figure 16), which causes large upwash effects at $r/R = 0.55$ but downwash effects in the vicinity of the location $r/R = 0.55$. The velocity contour indicates these effects in Figure 20. However, the increased local angle of attack caused by this upwash effects decreases the lift at $r/R = 0.55$, as seen from the results in Figure 18. The reason of this consequence can be interpreted as the critical stall angle is about 10° for the RISØ airfoil, which can be determined in 2D experimental airfoil characteristics, see the red point in Figure 19. Meanwhile, the current geometric angle of attack for the RISØ airfoil at $r/R = 0.55$ location is about 10°, as shown in Figure 14. The upwash effects induced by the counter-rotating vortices at $r/R = 0.55$ increase the geometric angle of attack (close to the critical angle of attack 10°), and the airfoil enters the stall regime. Because of

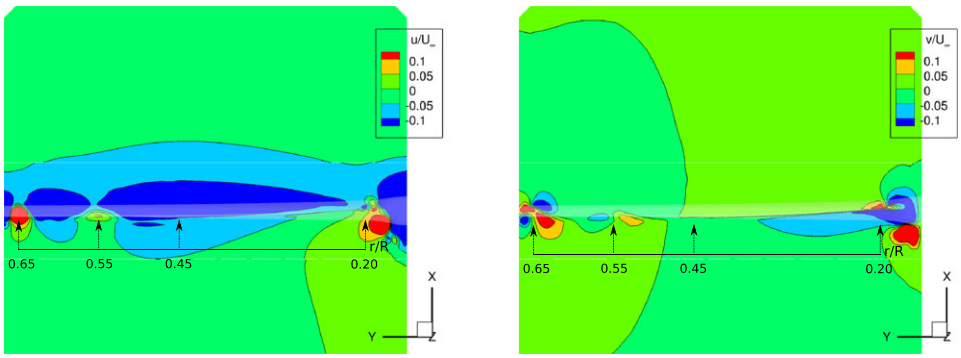

Figure 20. The vertical velocity u and spanwise velocity v contour in the plane $z = -0.20$ m behind blade 1, $\alpha_{0.35} = 5^{\circ}$.

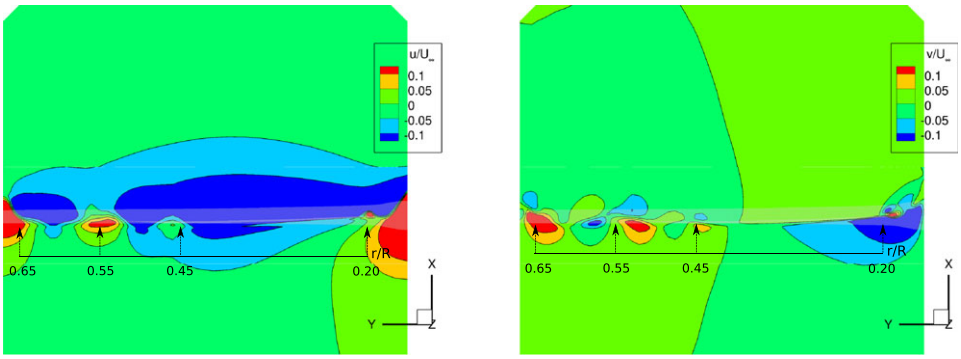

Figure 21. The vertical velocity u and spanwise velocity v contour in the plane $z = -0.20$ m behind blade 1, $\alpha_{0.35} = 8^{\circ}$.

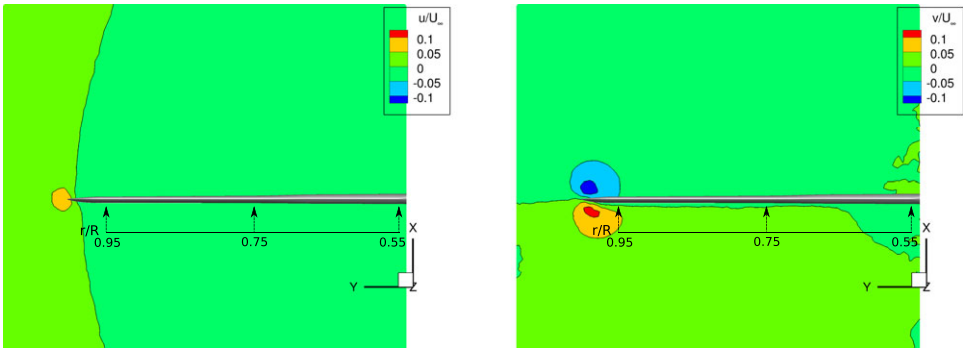

Figure 22. The vertical velocity u and spanwise velocity v contour in the plane $z = -0.20$ m behind blade 2, $\alpha_{0.60} = 5^{\circ}$.

the property of sharp aerodynamic characteristics of the RISØ airfoil, see the blue lift curve in Figure 19, lift decreases sharply in the stall regime. Therefore, the $r/R = 0.55$ section produces much smaller lift even with higher local angle of attack than 2D case. On the contrary, the RISØ airfoil section between $r/R = 0.60$ and $r/R = 0.65$ is, because of the downwash effects, at a reduced local angle of attack, which is within linear regime. Thus, the lift from 3D CFD at sections $r/R = 0.60 \sim 0.65$ is much lower than 2D.

When the geometric angle of attack increases to 8° at the $35\%R$ section, the comparison shows the maximum difference between 3D and 2D results has reduced to 27.3%, appearing at $r/R = 0.55$ on the RISØ airfoil section. In addition, 3D effects show little influence on the DU airfoil aerodynamic characteristics. From Figure 21, near the root region $r/R = 0.20$, less upwash effects can be observed compared with the case $\alpha_{0.35} = 5^{\circ}$. Therefore, as a result, C_L curve obtained from 3D results fits well with 2D experimental measurement. At $r/R = 0.55$, the difference between 3D CFD results and 2D

experimental values become smaller compared with the case $\alpha_{0.35} = 5^\circ$ even though this position has much stronger upwash effects, indicated by the velocity contour in Figure 21. The reason is that the geometric angle of attack of the RISØ airfoil at $r/R = 0.55$ is more than 13° from Figure 14, which is indicated by the green point in Figure 19. The $C_L - \alpha$ curve in this regime is generally flat without too much lift decrease if the angle of attack increases further. This leads to smaller difference found between 2D values and 3D results observed for the case $\alpha_{0.35} = 8^\circ$ compared with the case $\alpha_{0.35} = 5^\circ$. In the region $r/R = 0.60 \sim 0.65$, the downwash effect decreases the local angle of attack of the airfoil in the stall regime and increases the lift consequently.

For blade 2, the vertical and spanwise velocity field at the plane $z = -0.20$ m is shown in Figure 22. The strong tip vortex is clearly seen, and these tip effects are dominating the flow. A well-known effect of a tip vortex is the decrease of lift, which is in accordance with the results presented in Figure 15. No particularly unexpected loads distribution and velocity field are observed, and therefore, the influence of 3D effects on the airfoil characteristics of the blade 2 will not be discussed in this paper for the conciseness.

4. CONCLUSIONS

This paper presents the experimental and numerical investigations of MEXICO wind turbine blades. The quasi-2D aerodynamics characteristic of the non-rotating MEXICO blades are measured in the experiment, and the CFD simulations are carried out in order to better understand 3D flow around the blades. Eventually, more insight into MEXICO blades is given.

- For attached flow condition, the pressure distributions from the CFD calculations at three different sections compare well with the experimental measurements. Excellent match is observed at 92% spanwise section with the NACA airfoil profile. For the DU and RISØ airfoil sections, located at 35% and 60% span, respectively, a reasonable good agreement is found. Considerable difference is found on the suction side at the locations between $x/c = 0.15$ and $x/c = 0.34$ on the RISØ airfoil section. Besides, at $\alpha_{0.35} = 8^\circ$, the current computation does not capture the flow separation at the trailing edge.
- Experimental oil flow visualization has been compared with CFD limiting streamlines to investigate the flow topology for blade 3. Overall speaking, the separation line is well predicted by CFD, and hence, it indicates that the drag force along the blade is calculated reasonably in the condition $\alpha_{0.82} = 8^\circ$.
- The lift force distribution along the span is investigated for blades 1 and 2. Based on the results, it can be concluded that the intermediate region connecting the RISØ airfoil and the DU airfoil does not transit smoothly enough, which results in a sudden lift drop at $r/R = 0.55$ in both cases $\alpha_{0.35} = 5^\circ$ and $\alpha_{0.35} = 8^\circ$. However, the intermediate region connecting the RISØ airfoil and the NACA airfoil shows smooth lift distribution.
- By visualizing the flow field, large-scale vortical structures are observed over the suction side near the mid-span $r/R = 0.55$. The shed vorticity makes the flow three dimensional. In addition, a pair of counter-rotating vortices are found in the plane behind the blade 1 near the location $r/R = 0.55$. Compared with 3D CFD results, the upwash and downwash effects induced by these vortices significantly change the 2D aerodynamic characteristics of the RISØ airfoil family. Consequently 3D effects play an important role in the numerical modeling for calculating the aerodynamic loads for MEXICO rotor.

ACKNOWLEDGEMENT

The financial support of China Scholarship Council is gratefully acknowledged.

REFERENCES

1. Simms DA, Fingersh LJ, Jager DW, Cotrell JR, Schreck S, Larwood S. *Unsteady aerodynamics experiment phase VI: test configuration and available data campaigns*. National Renewable Energy Laboratory: Colorado, 2001.
2. Schepers J, Snel H, *Model experiments in controlled conditions. ECN Final Report ECN-E-07-042*, February, 2007.
3. Simms DA, Schreck S, Hand M, Fingersh LJ. *NREL Unsteady Aerodynamics Experiment in the NASA-Ames Wind Tunnel: a Comparison of Predictions to Measurements*. National Renewable Energy Laboratory: Colorado, 2001.
4. Schepers J, Boorsma K, Cho T, Gomez-Iradi S, Schaffarczyk P, Jeromin A, Shen W, Lutz T, Meister K, Stoevesandt B, et al. *Final report of IEA Task 29 Mexnext (Phase 1): Analysis of Mexico wind tunnel measurements*, Technical Report ECN-E12-004, Energy Research Center of the Netherlands, 2012.
5. Tsalicoglou C, Jafari S, Chokani N, Abhari RS. RANS Computations of Mexico rotor in uniform and yawed inflow. *Journal of Engineering for Gas Turbines and Power* 2014; **136**(1): 011202-1-011202-8.
6. Bechmann A, Srensen NN, Zahle F. CFD simulations of the MEXICO rotor. *Wind Energy* 2011; **14**: 677–89.

7. Srensen NN, Johansen J, Conway S, Srensen NN, Johansen J, Conway S, *CFD Computations of wind turbine blade loads during standstill operation KNOW-BLADE Task 3.1 report*, RISø National Laboratory Report, 2004.
8. Zhang Y, Alexander vZ, Gerard vB. Comparison of CFD simulations to non-rotating MEXICO blades experiment in the LTT wind tunnel of TUDelft. *Journal of Physics Conference Series* 2014; **524**: 012–013.
9. Farrell PE, Maddison JR. Conservative interpolation between volume meshes by local Galerkin projection. *Computer Methods in Applied Mechanics and Engineering* 2011; **200**: 89–100.
10. Menter F, Esch T. Elements of industrial heat transfer prediction. *16th Brazilian Congress of Mechanical Engineering (COBEM)*, Uberlandia, Brazil, 2001.
11. Patankar SV, Spalding DB. A calculation procedure for heat, mass and momentum transfer in three-dimensional parabolic flows. *International Journal of Heat and Mass Transfer* 1972; **15**: 1787–1806.
12. Hunt JC, Wray AA, Moin P. Eddies, streams, and convergence zones in turbulent flows. *In Studying Turbulence Using Numerical Simulation Databases* 1988; **2**(1): 193–208.
13. Anderson JD. *Fundamentals of Aerodynamics*. McGraw-Hill: Boston, USA, 2001.